Nuclear Instruments and Methods in Physics Research A 1089 (2026) 171602

Contents lists available at ScienceDirect

Nuclear Inst. and Methods in Physics Research, A

journal homepage: www.elsevier.com/locate/nima

Production and release of gaseous radionuclides from a tantalum-clad tungsten target at CSNS

Ping Xu [a,b], Qingbiao Wu [a,b,*], Zhiliang Hu [a,b], Yemian Li [a,b], Yuliang Zhang [a,b], Yinglin Ma [a,b], Sixuan Zhuang [a,b], Yufei Wang [a,b], Lun Li [a,b]

[a] *Institute of High Energy Physics, Chinese Academy of Sciences(CAS), Beijing, 100049, China*
[b] *Spallation Neutron Source Science Center(SNSSC), Dongguan, 523803, China*

ARTICLE INFO

Keywords:
Spallation neutron source
Tantalum-clad tungsten targets
Gaseous radionuclides
FLUKA simulation
HPGe gamma spectrometry

ABSTRACT

Spallation neutron sources produce gaseous radionuclides that constitute an important yet poorly constrained discharge-side source term, particularly for tantalum-clad tungsten targets. In this work, gaseous radionuclides in the high-activity off-gas of the China Spallation Neutron Source (CSNS, 1.6 GeV) were investigated by combining FLUKA Monte Carlo simulations with HPGe γ-spectrometric measurements at a monitoring point in the facility ventilation system. The measurements indicate that the discharged gaseous inventory is dominated by radioxenon, radiokrypton, and radioiodine. The simulations show that radioxenon, radiokrypton, and radioiodine isotopes are formed mainly during the evaporation stage of proton-induced spallation; therefore, the predicted activities of radioisotopes with half-lives longer than 1 h are only weakly dependent on the evaluated neutron-data library. Statistical comparison between the measured and simulated Xe/Kr radioisotopes indicates that the observed gaseous radionuclide pattern is primarily governed by the W-target source term. These results provide measurement-based constraints on gaseous source terms from a tantalum-clad tungsten spallation targets, with relevance to CTBT-related monitoring and off-gas management.

1. Introduction

Major spallation neutron sources worldwide include the Spallation Neutron Source (SNS, USA) [1,2], Japan Proton Accelerator Research Complex (J-PARC) [3,4], the China Spallation Neutron Source (CSNS) [5,6], the ISIS Neutron and Muon Source (ISIS, UK) [7,8], and the European Spallation Source (ESS, under construction) [9,10]. SNS employs a liquid-mercury target (Hg), and high-power mercury target technology has also been developed for J-PARC, whereas ISIS, CSNS and ESS adopt tungsten-based spallation targets. Under GeV-scale proton irradiation of heavy target materials, spallation and subsequent neutron activation generate a wide variety of radionuclides within both the target and surrounding media. Among them, inert noble gases (Xe, Kr) and volatile halogens (I, Br) are of particular concern due to their high mobility and potential for atmospheric release [11,12]. Compared with solid activation products, gaseous and volatile nuclides are more likely to migrate through ventilation/off-gas systems and contribute to routine releases, thereby directly influencing shielding design, delay-decay system performance, and discharge control from a radiological-protection perspective during operation.

In the context of nuclear-test monitoring and background discrimination, the CTBTO International Monitoring System (IMS) continuously tracks atmospheric radioxenon isotopes—typically ^{131m}Xe, ^{133}Xe, ^{133m}Xe, and ^{135}Xe [13,14]. Recent studies have shown that large nuclear installations and high-power spallation facilities can produce measurable contributions to regional xenon backgrounds, complicating source attribution and emphasizing the need for accurate radiological source-term characterization [15,16]. To date, experimental benchmarks for tungsten spallation cross sections remain scarce; accordingly, most studies rely on Monte Carlo–based radionuclide inventory predictions [17,18]. While the production of non-gaseous radionuclides has been assessed for spallation targets, discharge-side characterization of gaseous radionuclides from spallation neutron sources remains limited.

CSNS operates with a 1.6 GeV proton beam and has reached a target beam power of 160 kW, while the ongoing CSNS-II upgrade aims to further increase the beam power to 500 kW, making discharge-side characterization of gaseous radionuclides from tantalum-clad tungsten targets of direct engineering relevance [19]. In this work, the gaseous

---

[*] Corresponding author. Institute of High Energy Physics, Chinese Academy of Sciences(CAS), Beijing, 100049, China.
E-mail address: qbwu@ihep.ac.cn (Q. Wu).

https://doi.org/10.1016/j.nima.2026.171602
Received 15 January 2026; Received in revised form 30 March 2026; Accepted 18 April 2026

radionuclides produced in the CSNS (160 kW, 1.6 GeV) tungsten spallation target are studied through FLUKA simulations and γ-spectrometric measurements at the exhaust station. The objectives are to: (1) characterize the FLUKA-simulated production and activation of major radioxenon, radiokrypton, and radioiodine isotopes under a representative venting cycle; (2) identify and quantify the discharge-side radionuclide composition of activated gases based on γ-spectrometric measurements at the exhaust station; and (3) compare the simulated and measured Xe/Kr radionuclide patterns using a CMB/NNLS-based fitting framework, AICc-based model selection, and rank-based consistency analysis, in order to provide experimental constraints on discharge-side gaseous radionuclide compositions for solid tungsten spallation targets.

2. Principles and methods

2.1. HOG generation and release process at CSNS

The generation and release of high-activity off-gas (HOG) at CSNS can be conceptually divided into three stages (Fig. 1). (1) Nuclide production and transfer to the coolant: When the 1.6 GeV proton beam bombards the tungsten target, spallation reactions and secondary-neutron activation produce a variety of gaseous and volatile radionuclides, mainly radioxenon, radiokrypton, and radioiodine isotopes. These radionuclides diffuse from the target surface and transfer into the cooling circuit, either in dissolved form or as gas bubbles entrained in the circulating water. (2) Degassing and gas-phase accumulation in the surge tank: After condensation, the cooling water is collected in the surge tank, where the dissolved gaseous nuclides gradually degas from the liquid phase and accumulate in the gas phase. (3) Radiolytic gas buildup, venting, and delay decay: Under irradiation, water radiolysis generates H_2, O_2, H_2O_2, and various reactive radicals and hydrated species (H·, ·OH) [20,21]. When the H_2 volume fraction in the surge tank approaches its lower explosion limit (approximately 4%), the system automatically opens the vent valve, releasing the HOG into a decay tank for delayed decay treatment. Under current operating conditions, the surge tank and decay tank are alternately vented with a period of about 3.5 h, giving a total delay time of approximately 7 h. After decay, the off-gas passes through purification units—HEPA filters primarily removing aerosols and particulates, and optionally adsorbent beds for partial retention of reactive radioiodine species—before being discharged in a controlled manner to the exhaust stack.

2.2. FLUKA simulation of inert gas production

The CSNS spallation target adopts a single-wall container configuration (Fig. 1), consisting of a target vessel, a vessel cover plate, and multiple tungsten (W) plates mounted in parallel inside the vessel. The main target-station parameters are summarized in Table 1, and representative operating conditions of CSNS during the measurement period are described in the Appendix. Adjacent W plates are separated by cooling channels with gaps of 0.8–1.2 mm, and the coolant water flow rate is approximately 240 L min^{-1}. To reproduce the operational venting cycle, the buildup of gaseous radionuclides during 3.5 h of continuous proton irradiation was simulated.

Table 1
Target-station parameters of CSNS.

Technical parameter	CSNS value
Beam power, kW	160
Proton energy, GeV	1.6
Pulse repetition rate, Hz	25
Target and cladding material	Tungsten target with tantalum cladding
Tungsten target plate size (W × H)	170 mm × 70 mm
Reflector	Be/Fe
Target container material	S31603 stainless steel (316 L)
Cooling medium	Heavy water
Target replacement interval	3–5 years

Monte Carlo simulations were performed using FLUKA (version 4.5). Proton-induced spallation at 1.6 GeV was modeled using FLUKA's PEANUT framework, which describes the intranuclear cascade, pre-equilibrium emission, and subsequent statistical de-excitation (evaporation-dominated) on an event-by-event basis [22,23]. To assess uncertainties associated with low-energy nuclear data, neutron transport and activation calculations were performed using several evaluated nuclear data libraries, including JEFF-3.3, CENDL-3.1, BROND-3.1, ENDF/B-VIII.0, and JENDL-4.0u, while keeping the high-energy spallation models unchanged. Each simulation employed 128 parallel runs, with a total of 1E8 primary protons simulated per irradiation cycle.

2.3. Gamma-ray spectrometric measurement

During stable accelerator operation, HOG was sampled at each venting event (approximately 3.5 h interval) using a 5.12 L polyethylene sampling bag. γ-ray spectrometric measurements were conducted immediately after sampling using a p-type HPGe detector (GR5021, ORTEC) over 30 keV–2 MeV. Spectra were acquired in List Mode, in which spectroscopy data are streamed to the computer event-by-event without the acquire–store–clear–restart dead periods of standard histogram acquisition. The detector data were acquired continuously in list mode, and the recorded events were subsequently sorted into successive 5-min time bins for spectral analysis.

The detector full-energy peak efficiency was calibrated using ORTEC ANGLE (Advanced Gamma Spectroscopy Efficiency Calibration), which is based on the efficiency-transfer concept. In this method, a reference efficiency measured for a known configuration is transferred to the target geometry through solid-angle modeling and Monte Carlo calculation. The sampled gas was modeled as a uniformly distributed cylindrical volume source with dimensions matching the detector chamber

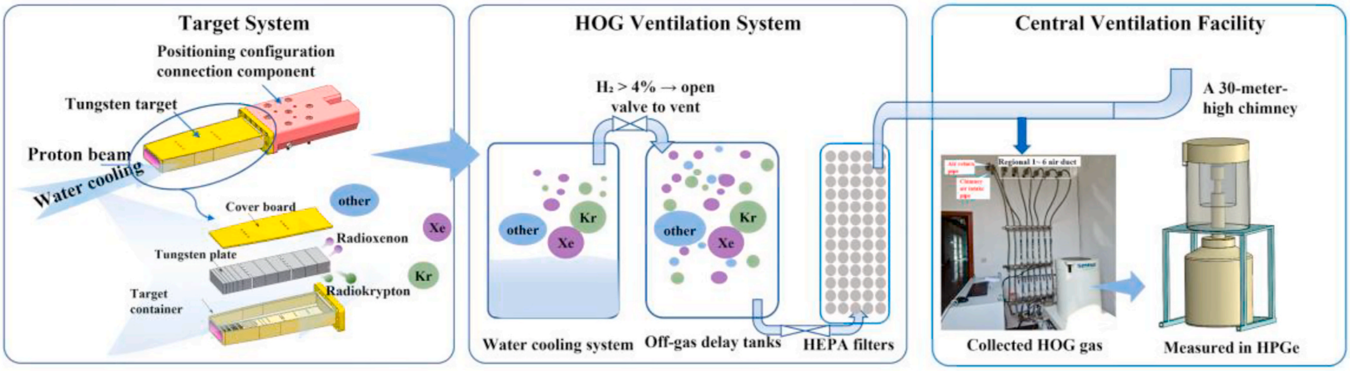

Fig. 1. The schematic of the HOG generation and release process.

geometry (13 cm in diameter and 10.0 cm in height). The efficiency calibration curve is shown in Fig. 2.

2.4. *Activity determination of gaseous radionuclides*

The gaseous radionuclides released in the HOG system are dominated by short-lived isotopes. Therefore, decay between sampling and γ-spectrometric counting must be corrected. Since the gas sampling duration was shorter than 1 min, decay during sampling was neglected. Two decay corrections were applied: (i) the cooling time between sampling and the start of counting (K_1) and (ii) decay during the counting interval (K_2) [24]:

$$K_1 = \frac{1}{e^{-\lambda t_1}} \tag{1}$$

$$K_2 = \frac{\lambda t_2}{1 - e^{-\lambda t_2}} \tag{2}$$

where λ is the decay constant of the radionuclide, t_1 is the delay time between sampling and measurement, and t_2 is the live counting time.

The activity concentration C_j of radionuclide j in the gas sample was calculated using:

$$C_j = K_1 K_2 \frac{N_{s,j}}{\varepsilon_j \eta_j V t_2} \tag{3}$$

where $N_{s,j}$ is the net peak count after background subtraction, ε_j is the full-energy peak detection efficiency, η_j is the γ-ray emission probability, V is the sample volume, and t_s is the sample counting time.

In γ-spectrometric measurements, counting statistics often dominate the total uncertainty. The statistical (counting) uncertainty of the net peak count can be evaluated from the sample and background spectra. The statistical uncertainty for each line-derived activity was calculated as:

$$\sigma_{N_{s,j}} = \sqrt{\frac{N_s}{{t_2}^2} + \frac{N_b}{{t_b}^2}} \tag{4}$$

where N_s and N_b denote the counting rates of the sample and background spectra, respectively, and t_b is the background measurement time.

Accordingly, the combined standard uncertainty of C_j is obtained by uncertainty propagation:

$$\left(\frac{u(C_j)}{C_j}\right)^2 = \left(\frac{\sigma_{N_{s,j}}}{N_{s,j}}\right)^2 + \left(\frac{u(\varepsilon_j)}{\varepsilon_j}\right)^2 + \left(\frac{u(V)}{V}\right)^2 \tag{5}$$

When multiple γ-lines were available for the same nuclide, the final activity was obtained as an inverse-variance weighted mean:

$$\overline{C_j} = \frac{\sum_{k=1}^{m} w_k C_{j,k}}{\sum_{k=1}^{m} w_k} \tag{6}$$

where $C_{j,k}$ is the activity concentration derived from the k-th γ-line of nuclide j, and the weights w_k are defined by:

$$w_k = \frac{1}{u^2(C_{j,k})} \tag{7}$$

The combined standard uncertainty of the weighted mean is then given by

$$u(\overline{C}_j) = \left(\sum_{k=1}^{m} w_k\right)^{-1/2} \tag{8}$$

If a γ-line was affected by known interferences (e.g., strong annihilation peak at/near 511 keV) or yielded activity estimates close to the detection limit, it was excluded from the weighted average to avoid bias; detection-limit considerations were evaluated following the Currie formalism [25].

2.5. *CMB/NNLS-based model comparison between FLUKA simulations and experimental measurements*

FLUKA provides radionuclide inventories in the target components, whereas the experimental observable is the gaseous activity concentration collected at the ventilation facility. A direct one-to-one conversion from FLUKA-calculated inventories (Bq) to measured exhaust gas concentrations (Bq·m^{-3}) was not attempted because transport/dilution parameters along the discharge pathway are not sufficiently characterized. Therefore, the comparison between simulations and measurements was performed within a model-based framework that focuses on radionuclide-pattern consistency rather than absolute magnitude.

A CMB/NNLS-based (Chemical Mass Balance/Non-Negative Least Squares) model was adopted to identify the dominant release-related controlling factor. Three candidate descriptors were considered for each material, namely total activity, surface-normalized activity, and volume-normalized activity density, under three source hypotheses: W-only, Ta-only, and joint W + Ta. For nuclide i, the measured gaseous activity concentration is denoted by M_i, and the corresponding FLUKA-calculated descriptors for W and Ta are denoted W_i by and Ta_i, respectively. The mixed-source model is written as

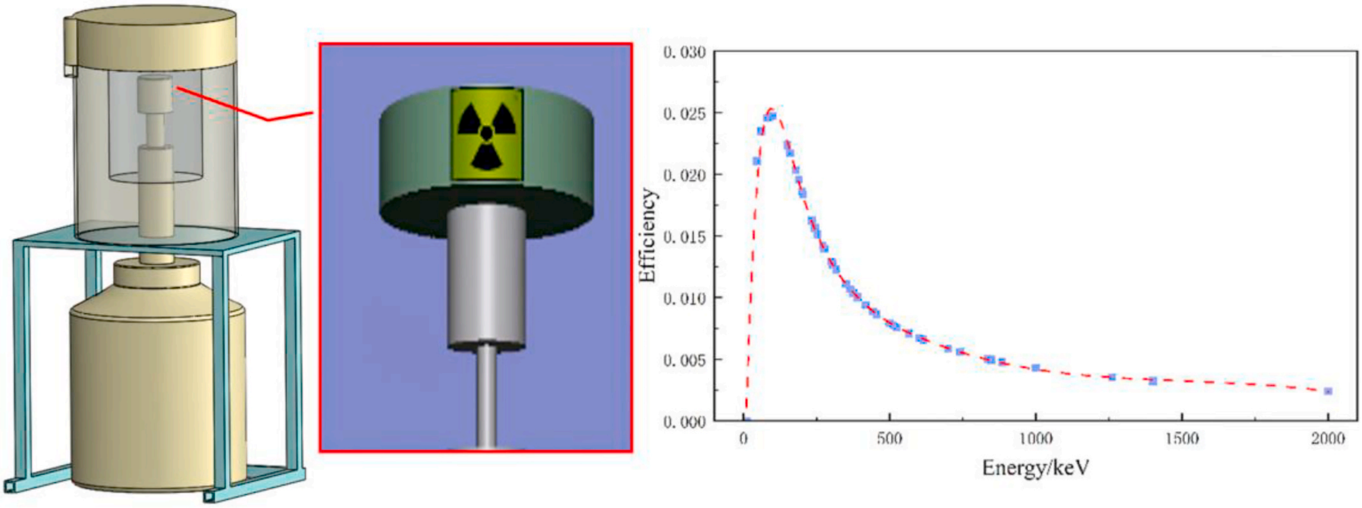

Fig. 2. Geometry used for absolute-efficiency calibration and the corresponding efficiency curve.

$$RSS = \min_{a,b\geq 0}\sum_{i}\left[log_{10}(M_i) - log_{10}(aW_i + bTa_i)\right]^2 \tag{9}$$

where a and b are non-negative scaling coefficients for W and Ta contributions, respectively, and RSS is the residual sum of squares on the logarithmic scale.

A CMB/NNLS-based model comparison was performed, and the candidate models were ranked using the corrected Akaike information criterion (AICc):

$$AICc = nln\left(\frac{RSS}{n}\right) + 2k + \frac{2k(k+1)}{n-k-1} \tag{10}$$

where n is the number of nuclides and k is the number of fitted parameters. In the present study, $k = 1$ for the single-source models (W-only or Ta-only) and $k = 2$ for the mixed-source model (W + Ta)。Lower values of AICc indicate better agreement between the model-predicted radionuclide pattern and the experimental measurements. AICc also penalizes unnecessary model complexity.

3. Results and analysis

3.1. FLUKA-simulated activities of Xe, I, and Kr radionuclides

3.1.1. Energy deposition and particle field characteristics in the CSNS target

Under 1.6 GeV proton irradiation of the tungsten target, Fig. 3(a)–(d) show the proton and neutron lethargy fluence spectra and the corresponding normalized spectral shapes at 11 plates along the beam direction (W-1 to W-11), while Fig. 3(e) presents the primary-particle energy-deposition distribution. The proton spectra (Fig. 3(a)) indicate a progressive decrease in fluence along the axis as inelastic interactions develop and beam energy is dissipated. From W-1 to W-11, the maximum proton energy decreases monotonically, reflecting the energy degradation of incident protons after strong hadronic interactions in the target. The normalized proton spectra (Fig. 3(c)) further show that, for W-1 to W-10, the proton fluence is dominated by the high-energy component (E > 100 MeV, accounting for >90%), whereas the high-energy fraction drops to ~83% at the last plate (W-11), indicating more pronounced spectral softening and depletion near the downstream end.

Taken together, the proton/neutron spectral features (progressive degradation and depletion of high-energy protons, neutron fluence dominated by MeV-scale components with only a minor high-energy tail) and the axial evolution of energy deposition suggest that, at 1.6 GeV, the dominant reaction mechanism in the tungsten target is governed by high-energy hadronic inelastic interactions, manifested as a spallation-driven cascade followed by statistical de-excitation (evaporation-dominated).

3.1.2. FLUKA-simulated activities of Xe, I, and Kr radioisotopes

Evaporation in tungsten spallation targets generates a broad suite of medium-mass fragments, while secondary MeV neutrons drive (n,xn) activation; therefore, radionuclide inventories are sensitive to neutron cross sections, branching ratios, and isomeric yields. Since FLUKA describes high-energy hadron–nucleus interactions through event-by-event physical models, while neutron transport and activation at lower energies rely on evaluated data libraries, this study compared the predictions obtained using five major databases: JEFF-3.3, CENDL-3.1, BROND-3.1, ENDF/B-VIII.0, and JENDL-4.0u. While short-lived radionuclides exhibit stronger sensitivity to database differences, longer-lived nuclides converge across libraries; the corresponding deviation maps of nuclide activities are shown in the Appendix.

Considering that a decay time of approximately 7 h is specified under the typical operating conditions of CSNS, this study focuses on radionuclides that remain significant contributors to the discharge-side gaseous source term within this time scale, namely Xe, I, and Kr radioisotopes with half-lives longer than 1 h. The calculated activities of these radionuclides obtained using different evaluated neutron cross-section libraries are shown in Fig. 4, aiming to assess the impact of nuclear-data uncertainties on the major gaseous radionuclide source term under realistic operating conditions. Fig. 4 presents the calculated activities of these radionuclides for a 3.5 h irradiation scenario, arranged in ascending order of half-life. The simulation results indicate that Xe

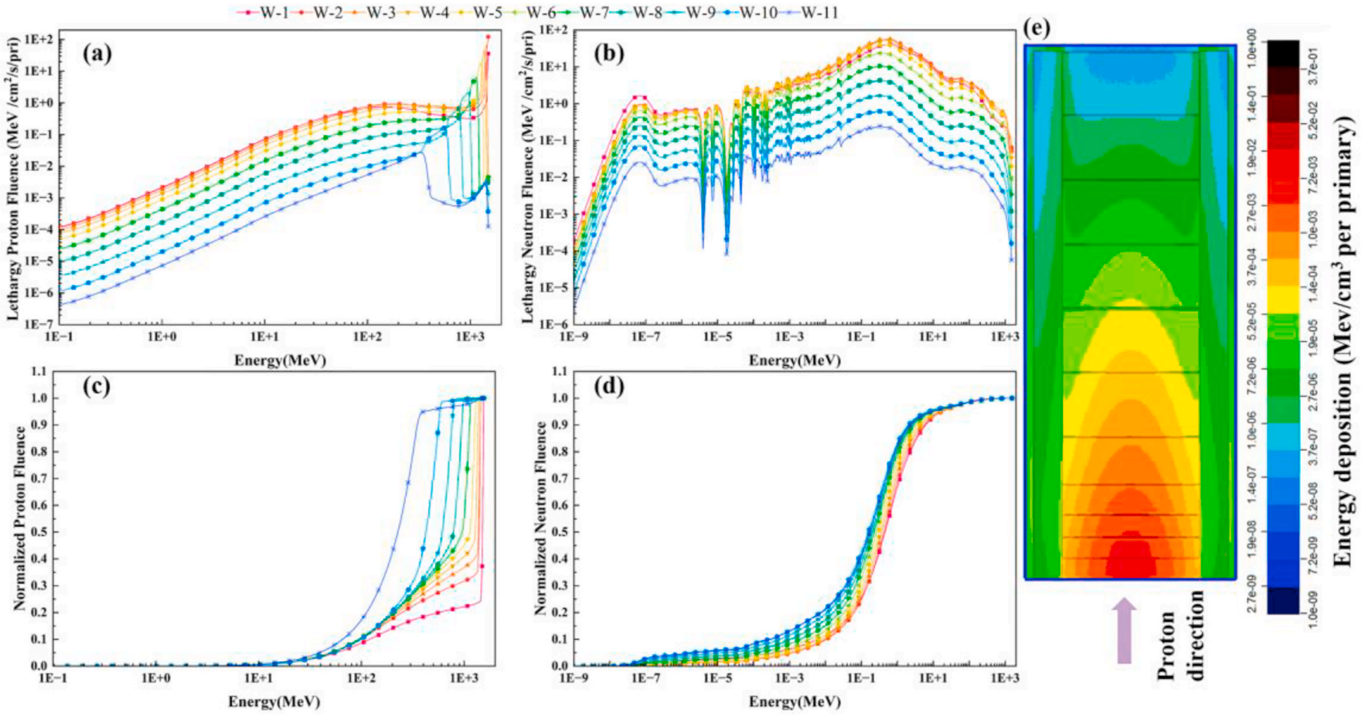

Fig. 3. Particle spectra and energy-deposition distributions: (a) and (b) proton and neutron lethargy fluence; (c) and (d) normalized proton and neutron fluence; (e) energy deposition.

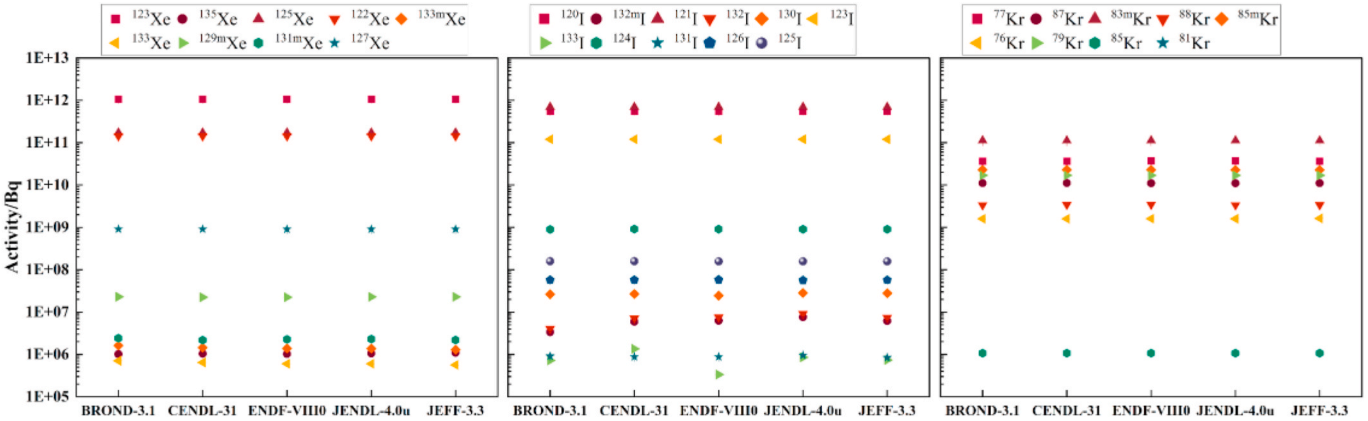

Fig. 4. Calculated activities of Xe (a), I (b), and Kr (c) radioisotopes produced in the tungsten target under different evaluated neutron cross-section libraries.

and I radioisotopes span approximately 1E5 to 1E13 Bq, while Kr radioisotopes span approximately1E2 to 1E12 Bq. For ^{81}Kr ($T_{1/2} = 2.29E5$ years), negligible accumulation occurs during the 3.5 h irradiation, yielding a very low activity (<1E3 Bq) and therefore a negligible contribution to the short-term discharge-side source term.

Overall, the FLUKA simulations indicate that under typical CSNS operating conditions, Xe and I radioisotopes dominate the discharge-side gaseous source term, whereas only a subset of Kr radioisotopes with intermediate half-lives is of engineering relevance during short-term operation. To ensure consistency and comparability in subsequent analyses, all quantitative results presented hereafter are based on calculations performed with the default JEFF-3.3 neutron cross-section library in FLUKA. The results obtained using other evaluated libraries are retained solely for assessing the uncertainty range associated with nuclear data and are not adopted as reference values.

3.1.3. Comparison of Xe, I, and Kr radioisotopes activities produced in the tungsten target and tantalum cladding

As the CSNS tungsten spallation target employs tantalum as a cladding material, the Ta layer is also subject to activation under irradiation by high-energy protons and secondary neutrons, potentially producing gaseous radionuclides such as Xe, I, and Kr. To evaluate the relative contributions of different structural materials to the discharge-side gaseous radiological source term, a comparative analysis of radionuclide activities generated in the tungsten target body and the tantalum cladding was performed. Fig. 5 presents the calculated activities of major noble-gas radioisotopes produced in the tungsten target and the tantalum cladding under identical irradiation conditions.

The results show that the activities of Xe, I, and Kr radioisotopes generated in the tungsten target are typically two to three orders of magnitude higher than those produced in the tantalum cladding. This pronounced difference primarily arises from the substantial disparity in geometric volume and effective production yield between the two components: the total volume of the tungsten target is approximately 7735 cm^3, whereas that of the tantalum cladding is only 78.5 cm^3. In a high-flux spallation neutron field, a larger target volume corresponds to a higher probability of nuclear reactions and a greater capacity for radionuclide accumulation.

3.2. Analysis of radionuclides in gaseous effluents by HPGe γ-ray spectrometry

To characterize gaseous radionuclides in the HOG under routine operation, gas samples were collected at the exhaust station and analyzed by HPGe γ-ray spectrometry for nuclide identification and activity concentration (Fig. 6). The measured activity concentrations are summarized in Table 2. The measured gaseous inventory is dominated by radioxenon, radiokrypton, and ^{41}Ar, with activity concentrations on the order of 1E3∼1E5 Bq·m^{-3}. Several radioxenon and radiokrypton isotopes were not identified in the measured spectra because no distinguishable γ-ray peaks were observed or because their emission intensities were too low, resulting in activity concentrations below the detection limit. Further details of the γ-spectrometric analysis are provided in the Appendix.

In addition to noble gases, several radioiodine isotopes (^{122}I, ^{123}I, ^{126}I, and ^{131}I) and one radiobromine isotope (^{76}Br) were identified. The activity of ^{122}I is comparable to that of its parent ^{122}Xe (ratio ≈ 1), which is consistent with in situ ingrowth during transport, sampling, and counting. Only a single radiobromine isotope was detected, and the measured ^{76}Br/^{76}Kr ratio is about 0.21. This observation suggests that ^{76}Br is more plausibly attributable to ingrowth from ^{76}Kr rather than to direct release from the target assembly.

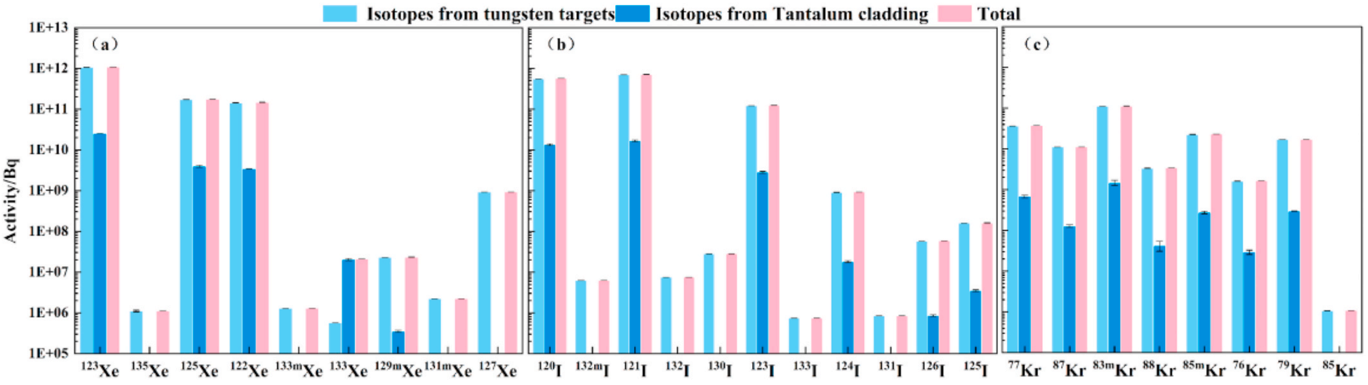

Fig. 5. Comparison of calculated activities of Xe, I, and Kr radionuclides produced in the tungsten target and the tantalum cladding at CSNS.

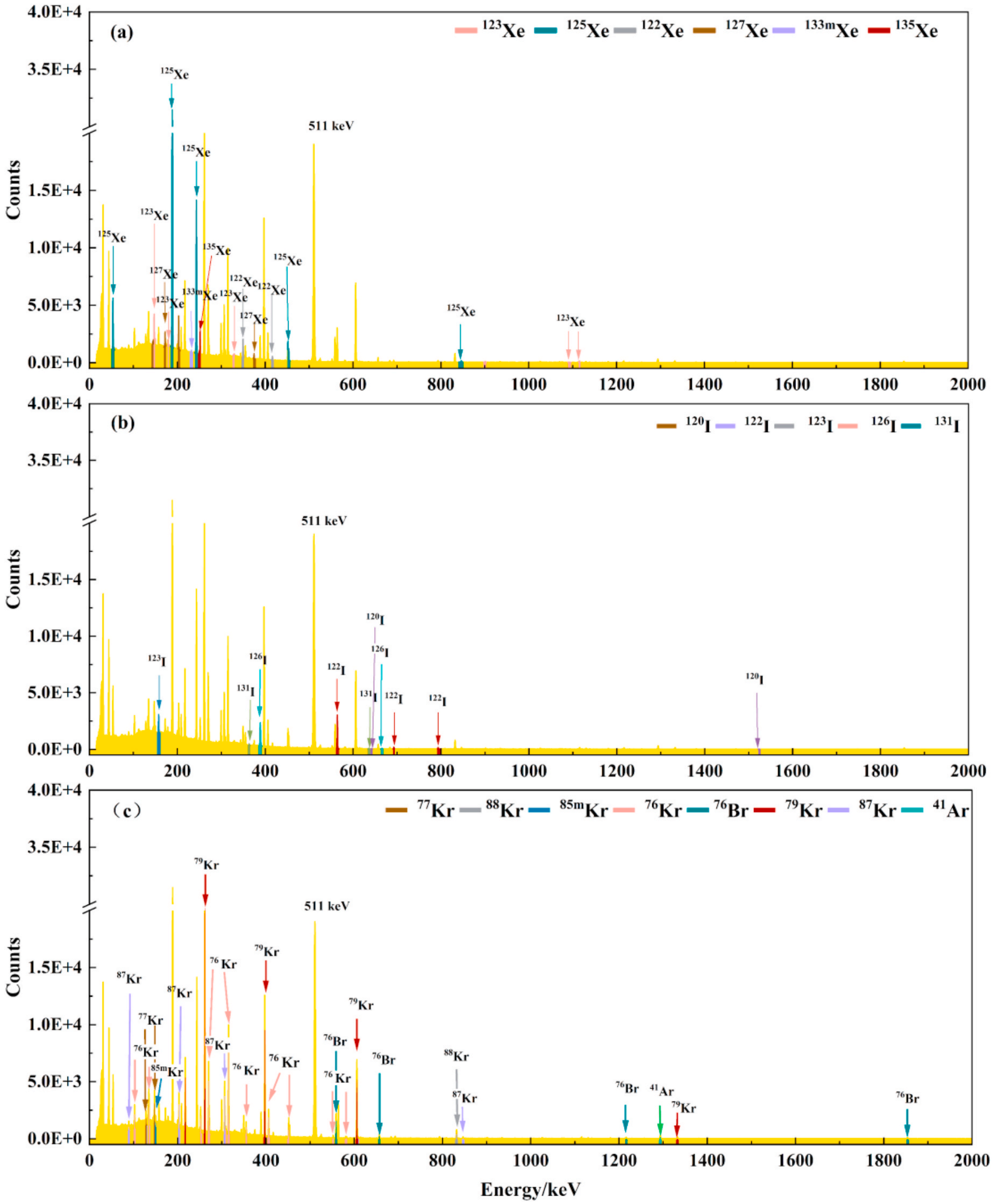

Fig. 6. γ spectra of the exhaust gas from the HOG system. (a), (b), and (c) show the full-energy γ-ray of radioxenon, radioiodine, and radiokrypton, respectively.

For halogen radionuclides, only a limited number of iodine isotopes were identified in the measured spectra, whereas no bromine signal that could be unambiguously attributed to direct release from the target system was observed. The average target-surface temperature recorded by the thermocouples is ~70 °C [26], a first-order estimate based on tabulated pure-substance vapor-pressure data suggests that, if halogens were present mainly as Br_2/I_2, volatility alone would not naturally explain a much weaker Br signature than I [27]. Under the present water-cooled target conditions, a more plausible explanation is aqueous speciation: bromine readily undergoes hydrolysis/disproportionation and is predominantly retained as hydrophilic Br^-/HOBr (and related oxybromine species), which enhances scrubbing and water-phase retention [28,29], while iodine may form a small fraction of more mobile gaseous species (e.g., I_2/HOI and organoiodine compounds) that can partition into the gas phase. Taken together, the observed I/Br contrast at the exhaust is more likely governed by wet-end chemical partitioning and retention, rather than by target-surface temperature alone. Because iodine can undergo complex transformations in the aqueous phase, the subsequent comparison between the measured results and the FLUKA predictions was restricted to Xe and Kr isotopes.

Table 2
Measured gaseous radionuclides in the ventilation facility system.

Radioisotopes	Half-life	γ-ray energy (keV)	Emission probability	Counting rate	Detection efficiency (%)	Activity concentration (Bq·m^{-3})	Relative uncertainty (%)
Radioxenon							
^{122}Xe	20.1 h	4.16E+02	1.90E-02	4.83E-02	9.50E-03	6.20E+04	1.77
^{123}Xe	2.05 h	1.78E+02	1.49E-01	9.17E-02	2.00E-02	8.98E+04	1.87
^{125}Xe	16.9 h	2.43E+02	2.88E-01	1.71E+00	1.56E-02	9.10E+04	0.21
^{127}Xe	36.3 d	3.75E+02	1.72E-01	6.61E-02	1.08E-02	7.01E+03	1.62
^{133m}Xe	2.20 d	2.33E+02	1.01E-01	8.14E-03	1.63E-02	1.03E+03	6.62
^{135}Xe	9.14 h	2.50E+02	9.60E-01	3.87E-02	1.54E-02	7.32E+02	5.42
Radioiodine							
^{120}I	1.36 h	5.60E+02	6.96E-01	3.12E-01	7.84E-03	1.13E+04	1.87
^{122}I	3.6 min	5.64E+02	1.80E-01	4.41E-01	7.84E-03	6.12E+04	0.43
^{123}I	13.2 h	1.59E+02	8.33E-01	1.99E-01	2.17E-02	2.77E+03	1.01
^{126}I	12.9 d	3.88E+02	2.90E-01	2.56E-01	1.05E-02	3.52E+04	0.23
^{131}I	8.03 d	3.64E+02	8.10E-01	1.17E-02	1.08E-02	2.68E+02	6.16
Radiokrypton							
^{76}Kr	14.8 h	2.70E+02	2.53E-01	9.06E-01	1.45E-02	6.06E+04	0.16
^{77}Kr	1.19 h	1.30E+02	8.10E-01	1.18E-01	2.38E-02	7.01E+03	1.71
^{79}Kr	35.0 h	2.61E+02	1.27E-01	3.30E+00	1.51E-02	3.72E+05	0.12
^{85m}Kr	4.48 h	3.04E+02	1.40E-01	5.80E-01	1.28E-02	1.25E+05	0.34
^{87}Kr	1.27 h	8.45E+02	7.34E-02	2.25E-03	5.00E-03	6.58E+03	3.14
^{88}Kr	2.83 h	8.35E+02	1.30E-01	1.94E-02	5.01E-03	1.57E+04	4.05
Other radionuclides							
^{76}Br	16.2 h	5.59E+02	7.40E-01	3.01E-01	7.84E-03	1.25E+04	0.31
^{41}Ar	1.83 h	1.29E+03	9.92E-01	7.31E-02	3.22E-03	1.14E+04	1.31

4. Comparison between FLUKA simulations and experimental measurements

To compare the FLUKA simulations with the HPGe measurements of Xe and Kr radioisotopes, both an AICc-based model comparison and a rank-based consistency analysis were performed. Fig. 7(a) presents the AICc-based comparison between the measured Xe/Kr activity concentrations and the FLUKA-simulated results for the target assembly. Nine candidate models were constructed by combining three release descriptors—total activity, surface-normalized activity, and activity density—with three source hypotheses: W-only, Ta-only, and combined W + Ta contributions. Among them, the lowest AICc is obtained for the total-activity + W-only model (AICc = 2.86), while the activity-density + W-only model also remains competitive (AICc = 3.49). By comparison, the surface-normalized models are much less favored, and the Ta-only models can be effectively excluded (AICc >10). These results do not merely indicate that W is the dominant production region; more importantly, they show that the FLUKA-predicted radionuclide inventory in W contains sufficient structure to account for the main features of the measured gaseous Xe/Kr pattern.

Fig. 7(b) further shows that the FLUKA-predicted radionuclide distribution in the W target is consistent with the measured relative ordering of Xe/Kr isotopes, with a Spearman rank correlation coefficient of $\rho = 0.83$ ($p < 1E\text{-}3$). This strong monotonic correlation indicates that the simulation reproduces the overall isotopic structure of the measured gaseous release pattern. Although the absolute release of individual nuclides may still be modified by transport and retention processes after production, the relative isotopic patterns of Xe and Kr remain well preserved. This is a stronger and more practically relevant conclusion than a simple source attribution, because it implies that FLUKA can be

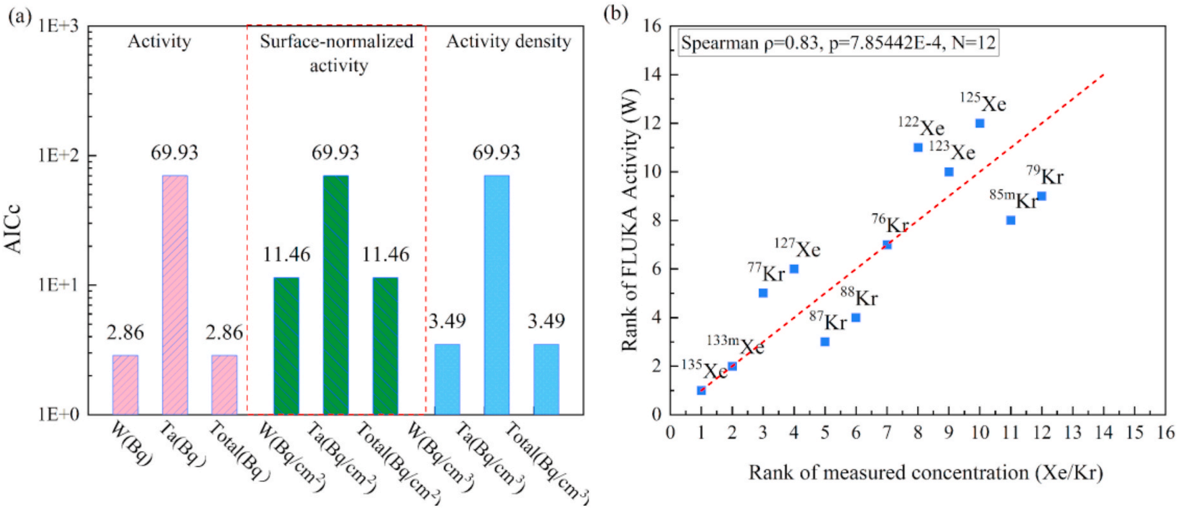

Fig. 7. Comparison between measured Xe/Kr activity concentrations and FLUKA-derived source descriptors for the target assembly: (a) AICc-based comparison of candidate models. (b) Rank–rank comparison based on Spearman correlation.

used to evaluate, at least semi-quantitatively, which noble-gas radionuclides are likely to dominate the discharge-side composition and whether the measured isotopic pattern is physically consistent with target-side production.

The observed agreement for Xe and Kr is physically reasonable. Under 1.6 GeV proton irradiation, tungsten undergoes high-energy hadronic reactions followed by statistical de-excitation, producing a broad range of noble-gas radionuclides. Because Xe and Kr are generated throughout the target bulk and exhibit extremely low solubility in metals, the discharge-side signal should be interpreted as the combined result of in-target production and subsequent migration/release processes, rather than as a direct one-to-one projection of the in-target inventory [30,31]. The better performance of the total-activity model therefore suggests that the measured Xe/Kr pattern is controlled mainly by the overall source strength in the W target.

The comparison also defines the scope of applicability of FLUKA. While FLUKA can predict radionuclide production and inventory in the target, it does not explicitly describe downstream processes such as release fraction, chemical retention, gas–liquid partitioning, and ventilation dilution. This limitation is especially important for reactive nuclides. The discrepancies observed for radioiodine and radiobromine at the facility ventilation system indicate that wet-system chemistry and retention play a major role in the water-cooled loop. Therefore, FLUKA can be regarded as a useful first-order evaluation tool for discharge-side Xe/Kr radionuclide patterns, but not as a complete predictive model for all gaseous species. A more direct simulation–measurement comparison for iodine and bromine would require additional treatment of chemical transformation and transport processes.

5. Conclusions

This study investigated gaseous radionuclides associated with a solid tungsten spallation target at CSNS (160 kW, 1.6 GeV) by combining FLUKA Monte Carlo simulations with HPGe γ-ray spectrometric measurements at the facility ventilation system. FLUKA predicts the production of a broad suite of Xe, Kr, and I radionuclides, with noble gases formed predominantly during statistical de-excitation. Under the CSNS delay–decay operation (approximately 7 h), radionuclides with half-lives longer than 1 h therefore dominate the discharged inventory.

The measurements show that the gaseous discharge is dominated by radioxenon and radiokrypton, whereas iodine exhibits larger simulation–measurement discrepancies, consistent with additional chemical retention and phase-transfer effects in the water-cooled target system. For chemically inert Xe and Kr, the measured isotopic pattern is in good agreement with the FLUKA-predicted W-target inventory. The statistical comparison further indicates that the exhaust-side Xe/Kr pattern is governed primarily by the overall source strength in the W target.

These results show that FLUKA cannot directly predict the absolute discharge concentration of all gaseous radionuclides, but it can provide a physically meaningful first-order evaluation of the discharge-side composition and isotopic pattern of noble gases in a water-cooled tungsten spallation target system. The present work therefore provides useful support for source-term screening, radionuclide ranking, and radiation-safety assessment at high-power spallation neutron facilities, while also offering relevant context for the interpretation of radioxenon observations in CTBT-related source attribution and background discrimination.

CRediT authorship contribution statement

Ping Xu: Conceptualization, Data curation, Formal analysis, Writing – original draft, Writing – review & editing. **Qingbiao Wu:** Conceptualization, Methodology, Supervision. **Zhiliang Hu:** Conceptualization, Methodology, Writing – review & editing. **Yemian Li:** Investigation, Methodology, Writing – review & editing. **Yuliang Zhang:** Project administration, Supervision, Writing – review & editing. **Yinglin Ma:** Writing – review & editing. **Sixuan Zhuang:** Writing – review & editing. **Yufei Wang:** Writing – review & editing. **Lun Li:** Writing – review & editing.

Declaration of competing interest

The authors declare that they have no known competing financial interests or personal relationships that could have appeared to influence the work reported in this paper.

Acknowledgements

This work was supported.

APPENDIX

1. Representative CSNS operating conditions during the measurement period

CSNS is a pulsed spallation neutron source operating at a repetition rate of 25 Hz. Publicly available information indicates that CSNS achieved stable 160 kW beam-on-target operation in March 2024. Although the beam power was briefly increased to 170 kW in 2024, routine operation in 2025 was maintained at 160 kW. This operating profile is representative of an extended user-operation period at CSNS.

To provide a more intuitive description of the operating conditions, a representative 24-h beam-on-target power history obtained from the official CSNS website is also included in the Appendix. The figure shows an effective beam-on-target time of 23.927 h within a 24-h period, indicating that beam interruptions during the representative operating interval were brief and infrequent. Accordingly, the gaseous releases observed in this work should be interpreted as characteristic of extended, quasi-continuous user operation with pulsed beam delivery, rather than isolated short-duration release events.

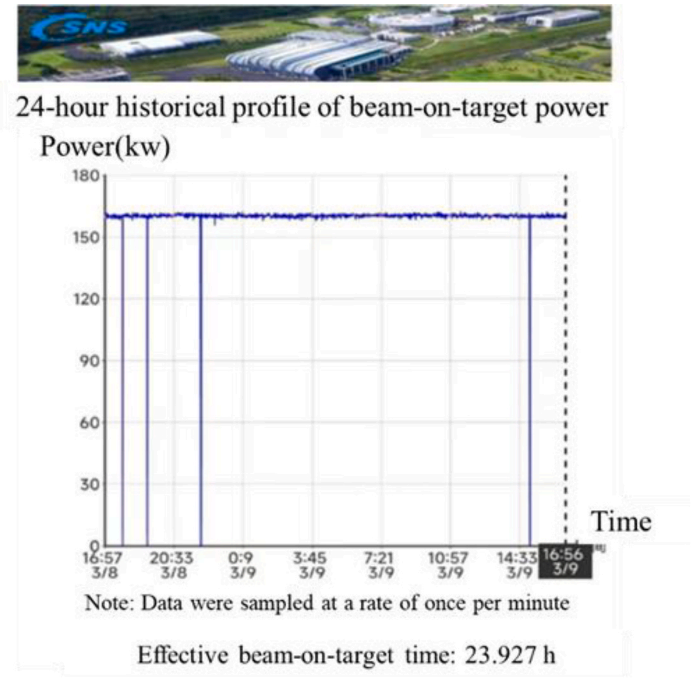

Fig. 1. 24-hour history of beam-on-target power.

2. Evaluation of nuclear-data uncertainty

Evaporation in tungsten spallation targets generates a broad suite of medium-mass fragments, while secondary MeV neutrons drive (n,xn) activation; therefore, radionuclide inventories are sensitive to neutron cross sections, branching ratios, and isomeric yields. Since FLUKA describes high-energy hadron–nucleus interactions through event-by-event physical models, while neutron transport and activation at lower energies rely on evaluated data libraries, this study compared the predictions obtained using five major databases: JEFF-3.3, CENDL-3.1, BROND-3.1, ENDF/B-VIII.0, and JENDL-4.0u. Taking JEFF-3.3 as the reference, Fig. 1 shows the deviation maps of nuclide activities relative to the baseline calculation, and Table 1 concluded the activities of all radioxenon, radiokrypton and radioiodine. As shown in Fig. 1, short-lived radionuclides exhibit stronger sensitivity to database differences, while results for longer-lived nuclides converge across libraries. This trend arises because, under fixed irradiation conditions, short-lived products approach a quasi-steady state dominated by instantaneous production rates, so any cross-section discrepancy is directly reflected in activity. In contrast, long-lived isotopes accumulate gradually during irradiation and cooling, averaging out part of the nuclear data variation.

Notably, among nuclides with half-lives exceeding 1 h, radioisotopes such as ^{133}Xe/^{133m}Xe/^{133}I, and ^{132}I/^{132m}I still display appreciable library dependence. Although these Xe and I radioisotopes primarily originate from medium-mass fragments formed in the proton-induced cascade–evaporation process at 1.6 GeV, the intense secondary neutron field within the target further redistributes their yields through (n,γ), (n,2n), and isomeric transition branching. Consequently, variations in neutron-induced reaction data and metastable branching ratios among different evaluated libraries lead to noticeable differences in the predicted radioiodine isotope activities.

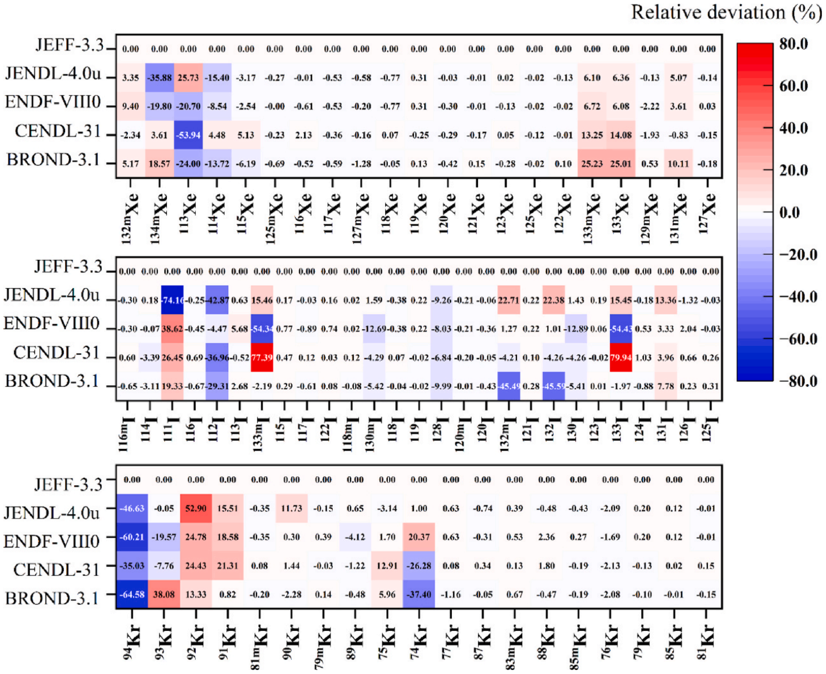

	^{132m}Xe	^{134m}Xe	^{113}Xe	^{114}Xe	^{115}Xe	^{125m}Xe	^{116}Xe	^{117}Xe	^{127m}Xe	^{118}Xe	^{119}Xe	^{120}Xe	^{121}Xe	^{123}Xe	^{125}Xe	^{122}Xe	^{133m}Xe	^{133}Xe	^{129m}Xe	^{131m}Xe	^{127}Xe
JEFF-3.3	0.00	0.00	0.00	0.00	0.00	0.00	0.00	0.00	0.00	0.00	0.00	0.00	0.00	0.00	0.00	0.00	0.00	0.00	0.00	0.00	0.00
JENDL-4.0u	3.35	-35.88	25.73	-15.40	-3.17	-0.27	-0.01	-0.53	-0.58	-0.77	0.31	-0.03	-0.01	0.02	-0.02	-0.13	6.10	6.36	-0.13	5.07	-0.14
ENDF-VIII0	9.40	-19.80	-20.70	-8.54	-2.54	-0.00	-0.61	-0.53	-0.20	-0.77	0.31	-0.30	-0.01	-0.13	-0.02	-0.02	6.72	6.08	-2.22	3.61	0.03
CENDL-31	-2.34	3.61	-53.94	4.48	5.13	-0.23	2.13	-0.36	-0.16	0.07	-0.25	-0.29	-0.17	0.05	-0.12	-0.01	13.25	14.08	-1.93	-0.83	-0.15
BROND-3.1	5.17	18.57	-24.00	-13.72	-6.19	-0.69	-0.52	-0.59	-1.28	-0.05	0.13	-0.42	0.15	-0.28	-0.02	0.10	25.23	25.01	0.53	10.11	-0.18

	^{116m}I	^{114}I	^{111}I	^{116}I	^{112}I	^{113}I	^{133m}I	^{115}I	^{117}I	^{122}I	^{118m}I	^{130m}I	^{118}I	^{119}I	^{128}I	^{120m}I	^{120}I	^{132m}I	^{121}I	^{132}I	^{130}I	^{123}I	^{133}I	^{124}I	^{131}I	^{126}I	^{125}I
JEFF-3.3	0.00	0.00	0.00	0.00	0.00	0.00	0.00	0.00	0.00	0.00	0.00	0.00	0.00	0.00	0.00	0.00	0.00	0.00	0.00	0.00	0.00	0.00	0.00	0.00	0.00	0.00	0.00
JENDL-4.0u	-0.30	0.18	-74.16	-0.25	-42.87	0.63	15.46	0.17	-0.03	0.16	0.02	1.59	-0.38	0.22	-9.26	-0.21	-0.06	22.71	0.22	22.38	1.43	0.19	15.45	-0.18	13.36	-1.32	-0.03
ENDF-VIII0	-0.30	-0.07	38.62	-0.45	-4.47	5.68	-54.34	0.77	-0.89	0.74	0.02	-12.69	-0.38	0.22	-8.03	-0.21	-0.36	1.27	0.22	1.01	-12.89	0.06	-54.43	0.53	3.33	2.04	-0.03
CENDL-31	0.60	-3.39	26.45	0.69	-36.96	-0.52	77.39	0.47	0.12	0.03	0.12	-4.29	0.07	-0.02	-6.84	-0.20	-0.05	-4.21	0.10	-4.26	-4.26	-0.02	79.94	1.03	3.96	0.66	0.26
BROND-3.1	-0.65	-3.11	19.33	-0.67	-29.31	2.68	-2.19	0.29	-0.61	0.08	-0.08	-5.42	-0.04	-0.02	-9.99	-0.01	-0.43	-45.49	0.28	-45.59	-5.41	0.01	-1.97	-0.88	7.78	0.23	0.31

	^{94}Kr	^{93}Kr	^{92}Kr	^{91}Kr	^{81m}Kr	^{90}Kr	^{79m}Kr	^{89}Kr	^{75}Kr	^{74}Kr	^{77}Kr	^{87}Kr	^{83m}Kr	^{88}Kr	^{85m}Kr	^{76}Kr	^{79}Kr	^{85}Kr	^{81}Kr
JEFF-3.3	0.00	0.00	0.00	0.00	0.00	0.00	0.00	0.00	0.00	0.00	0.00	0.00	0.00	0.00	0.00	0.00	0.00	0.00	0.00
JENDL-4.0u	-46.63	-0.05	52.90	15.51	-0.35	11.73	-0.15	0.65	-3.14	1.00	0.63	-0.74	0.39	-0.48	-0.43	-2.09	0.20	0.12	-0.01
ENDF-VIII0	-60.21	-19.57	24.78	18.58	-0.35	0.30	0.39	-4.12	1.70	20.37	0.63	-0.31	0.53	2.36	0.27	-1.69	0.20	0.12	-0.01
CENDL-31	-35.03	-7.76	24.43	21.31	0.08	1.44	-0.03	-1.22	12.91	-26.28	0.08	0.34	0.13	1.80	-0.19	-2.13	-0.13	0.02	0.15
BROND-3.1	-64.58	38.08	13.33	0.82	-0.20	-2.28	0.14	-0.48	5.96	-37.40	-1.16	-0.05	0.67	-0.47	-0.19	-2.08	-0.10	-0.01	-0.15

Fig. 2. Relative deviations of radionuclide activities calculated with different neutron cross-section libraries (compared to JEFF-3.3).

Table 1
FLUKA simulated gaseous radionuclides in the tantalum-clad tungsten target at CSNS

Radioisotopes	Half-life (s)	Activity in W(after 3.5h irradiation) (Bq)	Activity in Ta(after 3.5h irradiation) (Bq)	Activity in W(after 7h decay) (Bq)	Activity in Ta(after 7h decay) (Bq)
^{94}Kr	2.12E-01	3.01E+07	0.00E+00	0.00E+00	0.00E+00
^{93}Kr	1.29E+00	1.78E+07	0.00E+00	0.00E+00	0.00E+00
^{92}Kr	1.84E+00	2.47E+07	0.00E+00	0.00E+00	0.00E+00
^{91}Kr	8.57E+00	8.17E+07	0.00E+00	0.00E+00	0.00E+00
^{81m}Kr	1.31E+01	1.08E+11	1.57E+09	0.00E+00	0.00E+00
^{90}Kr	3.23E+01	3.41E+08	0.00E+00	6.59E-227	0.00E+00
^{79m}Kr	5.00E+01	7.62E+10	1.27E+09	1.45E-141	2.43E-143
^{89}Kr	1.89E+02	9.80E+08	1.37E+07	7.15E-32	9.99E-34
^{75}Kr	2.76E+02	2.39E+08	0.00E+00	7.80E-20	0.00E+00
^{74}Kr	6.90E+02	2.06E+07	3.82E+08	2.08E-04	3.88E-03
^{77}Kr	4.28E+03	2.35E+10	8.75E+07	3.95E+08	1.47E+06
^{87}Kr	4.58E+03	7.24E+09	9.12E+08	1.60E+08	2.01E+07
^{83m}Kr	6.59E+03	7.23E+10	1.64E+07	5.10E+09	1.16E+06
^{88}Kr	1.02E+04	2.21E+09	1.60E+08	3.97E+08	2.88E+07
^{85m}Kr	1.61E+04	1.47E+10	1.62E+07	4.98E+09	5.47E+06
^{76}Kr	5.33E+04	1.02E+09	1.81E+08	7.33E+08	1.31E+08
^{79}Kr	1.26E+05	1.08E+10	7.70E+03	9.43E+09	6.71E+03
^{85}Kr	3.39E+08	6.96E+05	4.32E+00	6.96E+05	4.32E+00
^{81}Kr	7.22E+12	2.92E+02	0.00E+00	2.92E+02	0.00E+00
^{116m}I	3.27E-06	2.20E+10	5.70E+08	0.00E+00	0.00E+00
^{114}I	2.10E+00	3.91E+09	1.06E+08	0.00E+00	0.00E+00
^{111}I	2.50E+00	3.22E+07	0.00E+00	0.00E+00	0.00E+00
^{116}I	2.91E+00	4.89E+10	1.29E+09	0.00E+00	0.00E+00
^{112}I	3.34E+00	5.07E+07	0.00E+00	0.00E+00	0.00E+00
^{113}I	6.60E+00	2.56E+09	5.89E+07	0.00E+00	0.00E+00
^{133m}I	9.00E+00	7.54E+06	0.00E+00	0.00E+00	0.00E+00
^{115}I	9.00E+01	1.68E+10	4.11E+08	8.67E-75	2.12E-76
^{117}I	1.33E+02	1.16E+11	2.96E+09	1.29E-46	3.31E-48
^{122}I	2.18E+02	1.73E+11	3.96E+09	2.56E-24	5.86E-26
^{118m}I	5.10E+02	5.04E+10	1.31E+09	6.74E-05	1.75E-06
^{130m}I	5.30E+02	3.92E+07	0.00E+00	1.96E-07	0.00E+00
^{118}I	8.22E+02	1.12E+11	2.92E+09	6.63E+01	1.72E+00
^{119}I	1.15E+03	3.85E+11	9.24E+09	9.25E+04	2.22E+03
^{128}I	1.50E+03	8.32E+08	9.76E+06	7.26E+03	8.51E+01
^{120m}I	3.18E+03	8.53E+10	1.93E+09	3.51E+08	7.96E+06
^{120}I	4.90E+03	3.42E+11	8.36E+09	9.64E+09	2.36E+08
^{132m}I	4.99E+03	9.68E+06	0.00E+00	2.93E+05	0.00E+00
^{121}I	7.63E+03	4.34E+11	1.04E+10	4.40E+10	1.05E+09

(*continued on next page*)

Table 1 (*continued*)

Radioisotopes	Half-life (s)	Activity in W(after 3.5h irradiation) (Bq)	Activity in Ta(after 3.5h irradiation) (Bq)	Activity in W(after 7h decay) (Bq)	Activity in Ta(after 7h decay) (Bq)
^{132}I	**8.26E+03**	**1.15E+07**	**0.00E+00**	**1.39E+06**	**0.00E+00**
^{130}I	**4.45E+04**	**4.03E+07**	**0.00E+00**	**2.72E+07**	**0.00E+00**
^{123}I	**4.76E+04**	**7.56E+10**	**1.75E+09**	**5.24E+10**	**1.21E+09**
^{133}I	**7.50E+04**	**1.72E+06**	**0.00E+00**	**1.36E+06**	**0.00E+00**
^{124}I	**3.61E+05**	**6.34E+08**	**1.06E+07**	**6.04E+08**	**1.01E+07**
^{131}I	**6.93E+05**	**1.37E+06**	**0.00E+00**	**1.34E+06**	**0.00E+00**
^{126}I	**1.12E+06**	**1.45E+08**	**7.26E+05**	**1.43E+08**	**7.15E+05**
^{125}I	**5.13E+06**	**1.00E+08**	**2.16E+06**	**1.00E+08**	**2.15E+06**
^{129}I	**4.95E+14**	**1.71E+04**	**0.00E+00**	**1.71E+04**	**0.00E+00**
^{132m}Xe	**8.39E-03**	**9.26E+07**	**0.00E+00**	**0.00E+00**	**0.00E+00**
^{134m}Xe	**2.90E-01**	**7.87E+06**	**0.00E+00**	**0.00E+00**	**0.00E+00**
^{113}Xe	**2.74E+00**	**1.10E+07**	**0.00E+00**	**0.00E+00**	**0.00E+00**
^{114}Xe	**1.00E+01**	**1.08E+08**	**0.00E+00**	**0.00E+00**	**0.00E+00**
^{115}Xe	**1.80E+01**	**7.91E+08**	**2.88E+07**	**0.00E+00**	**0.00E+00**
^{125m}Xe	**5.70E+01**	**3.78E+10**	**7.81E+08**	**3.09E-123**	**6.39E-125**
^{116}Xe	**5.90E+01**	**5.09E+09**	**1.52E+08**	**1.35E-119**	**4.04E-121**
^{117}Xe	**6.10E+01**	**1.76E+10**	**5.01E+08**	**7.67E-115**	**2.19E-116**
^{127m}Xe	**6.92E+01**	**8.26E+09**	**1.42E+08**	**1.96E-100**	**3.38E-102**
^{118}Xe	**2.28E+02**	**6.19E+10**	**1.61E+09**	**3.31E-23**	**8.59E-25**
^{119}Xe	**3.48E+02**	**1.49E+11**	**3.70E+09**	**2.37E-11**	**5.88E-13**
^{120}Xe	**2.40E+03**	**3.71E+11**	**9.28E+09**	**2.56E+08**	**6.41E+06**
^{121}Xe	**2.41E+03**	**5.65E+11**	**1.38E+10**	**3.97E+08**	**9.69E+06**
^{123}Xe	**7.38E+03**	**6.59E+11**	**1.56E+10**	**6.18E+10**	**1.46E+09**
^{125}Xe	**6.08E+04**	**1.08E+11**	**2.45E+09**	**8.08E+10**	**1.84E+09**
^{122}Xe	**7.24E+04**	**8.98E+10**	**2.14E+09**	**7.06E+10**	**1.68E+09**
^{133m}Xe	**1.90E+05**	**8.36E+05**	**0.00E+00**	**7.63E+05**	**0.00E+00**
^{133}Xe	**4.53E+05**	**3.54E+05**	**0.00E+00**	**3.40E+05**	**0.00E+00**
^{129m}Xe	**7.67E+05**	**4.65E+07**	**1.30E+05**	**4.55E+07**	**1.27E+05**
^{131m}Xe	**1.02E+06**	**1.53E+06**	**0.00E+00**	**1.51E+06**	**0.00E+00**
^{127}Xe	**3.14E+06**	**6.18E+08**	**1.27E+07**	**6.14E+08**	**1.26E+07**

3. Analysis of radionuclides in gaseous effluents by HPGe γ-ray spectrometry

Details of the γ-spectrometric analysis of gaseous radionuclides are summarized in Table 2. In the present study, many radionuclides emit multiple γ rays. For activity determination, priority was therefore given to a single full-energy peak that could be clearly identified and was free from obvious spectral interference or peak overlap. Activities derived from other available full-energy peaks were used for cross-checking, while the final reported activity concentration was based primarily on the selected interference-free peak.

For radiokrypton isotopes ^{83}Kr ($E_\gamma = 9.4$ keV, $I_\gamma = 5.\ 5\%$); and several radioxenon isotopes, including ^{131m}Xe ($E_\gamma = 163.9$ keV, $I_\gamma = 1.95\%$), ^{133}Xe ($E_\gamma = 81.0$ keV, $I_\gamma = 36.9\%$), and ^{129m}Xe ($E_\gamma = 39.57$ keV, $I_\gamma = 7.5\%$; $E_\gamma = 196.56$ keV, $I_\gamma = 4.59\%$), the observed deviations are likely associated with low-energy emissions and/or weak γ-ray intensities, which reduce detection efficiency and may place some activities close to, or below, the HPGe detection limit.

The situation for radioiodine is more complex. For some iodine radionuclides, no clearly distinguishable full-energy peaks could be identified in the measured spectra. For example, ^{130}I ($E_\gamma = 536.066$ keV, $I_\gamma = 99\%$; $E_\gamma = 668.536$ keV, $I_\gamma = 96\%$), and ^{132}I ($E_\gamma = 667.71$ keV, $I_\gamma = 98.7\%$; $E_\gamma = 772.6$ keV, $I_\gamma = 75.6\%$) were observed. This absence is consistent with the more complex aqueous chemistry of iodine in the water-cooled system, which may enhance retention in the liquid phase and on wetted surfaces, thereby reducing the effective gaseous release and causing the corresponding activities to remain below the practical detection limit.

Table 2
Measured gaseous radionuclides in the ventilation facility system

Radioisotopes	Half-life	Decay correction factor	γ-ray energy/KeV	Emission probability	Total counts	Counting time/s	Count rate	Detection efficiency(%)	Activity concentration(Bq/m3)	RE. (%)
^{122}Xe	**20.1h**	**1.18E+00**	**4.16E+02**	**1.90E-02**	**1.74E+03**	**3.60E+04**	**4.83E-02**	**9.50E-03**	**6.20E+04**	**1.77**
^{123}Xe	**2.05h**	**1.49E+01**	**1.78E+02**	**1.49E-01**	**3.30E+03**	**3.60E+04**	**9.17E-02**	**2.00E-02**	**8.98E+04**	**1.87**
^{125}Xe	**16.9h**	**1.22E+00**	**2.43E+02**	**2.88E-01**	**6.15E+04**	**3.60E+04**	**1.71E+00**	**1.56E-02**	**9.10E+04**	**0.21**
^{127}Xe	**36.3d**	**1.00E+00**	**3.75E+02**	**1.72E-01**	**2.38E+03**	**3.60E+04**	**6.61E-02**	**1.08E-02**	**7.01E+03**	**1.62**
^{133m}Xe	**2.20d**	**1.07E+00**	**2.33E+02**	**1.01E-01**	**2.93E+02**	**3.60E+04**	**8.14E-03**	**1.63E-02**	**1.03E+03**	**6.62**
^{135}Xe	**9.14h**	**1.43E+00**	**2.50E+02**	**9.60E-01**	**1.39E+03**	**3.60E+04**	**3.87E-02**	**1.54E-02**	**7.32E+02**	**5.42**
^{76}Kr	**14.8h**	**1.25E+00**	**2.70E+02**	**2.53E-01**	**3.26E+04**	**3.60E+04**	**9.06E-01**	**1.45E-02**	**6.06E+04**	**0.16**
^{77}Kr	**1.19h**	**5.84E+00**	**1.30E+02**	**8.10E-01**	**4.25E+03**	**3.60E+04**	**1.18E-01**	**2.38E-02**	**7.01E+03**	**1.71**
^{79}Kr	**35.0h**	**1.10E+00**	**2.61E+02**	**1.27E-01**	**1.19E+05**	**3.60E+04**	**3.30E+00**	**1.51E-02**	**3.72E+05**	**0.12**
^{85m}Kr	**4.48h**	**1.97E+00**	**3.04E+02**	**1.40E-01**	**2.09E+04**	**3.60E+04**	**5.80E-01**	**1.28E-02**	**1.25E+05**	**0.34**
^{87}Kr	**1.27h**	**5.47E+00**	**8.45E+02**	**7.34E-02**	**8.10E+01**	**3.60E+04**	**2.25E-03**	**5.00E-03**	**6.58E+03**	**3.14**
^{88}Kr	**2.83h**	**2.68E+00**	**8.35E+02**	**1.30E-01**	**6.99E+02**	**3.60E+04**	**1.94E-02**	**5.01E-03**	**1.57E+04**	**4.05**
^{120}I	**1.36h**	**1.01E+00**	**5.60E+02**	**6.96E-01**	**1.12E+04**	**3.60E+04**	**3.12E-01**	**7.84E-03**	**1.13E+04**	**1.87**
^{122}I	**3.63min**	**/**	**5.64E+02**	**1.80E-01**	**1.59E+04**	**3.60E+04**	**4.41E-01**	**7.84E-03**	**6.12E+04**	**0.43**
^{123}I	**13.2h**	**1.29E+00**	**1.59E+02**	**8.33E-01**	**7.16E+03**	**3.60E+04**	**1.99E-01**	**2.17E-02**	**2.77E+03**	**1.01**
^{126}I	**12.9d**	**1.01E+00**	**3.88E+02**	**2.90E-01**	**9.20E+03**	**3.60E+04**	**2.56E-01**	**1.05E-02**	**3.52E+04**	**0.23**

(*continued on next page*)

Table 2 (*continued*)

Radioisotopes	Half-life	Decay correction factor	γ-ray energy/KeV	Emission probability	Total counts	Counting time/s	Count rate	Detection efficiency(%)	Activity concentration(Bq/m3)	RE. (%)
^{131}I	**8.02d**	**1.02E+00**	**3.64E+02**	**8.10E-01**	**4.22E+02**	**3.60E+04**	**1.17E-02**	**1.08E-02**	**2.68E+02**	**6.16**
^{76}Br	**16.2h**	**1.23E+00**	**5.59E+02**	**7.40E-01**	**1.08E+04**	**3.60E+04**	**3.01E-01**	**7.84E-03**	**1.25E+04**	**0.31**
^{41}Ar	**1.83h**	**3.88E+00**	**1.29E+03**	**9.92E-01**	**2.63E+03**	**3.60E+04**	**7.31E-02**	**3.22E-03**	**1.74E+04**	**1.31**

Data availability

Data will be made available on request.

References

[1] S. Henderson, et al., Nucl. Instrum. Methods Phys. Res. A 763 (2014) 610–673, https://doi.org/10.1016/j.nima.2014.03.067.

[2] G.S. Bauer, Nucl. Instrum. Methods Phys. Res. A 463 (2001) 505–543, https://doi.org/10.1016/S0168-9002(01)00167-X.

[3] Y. Ikeda, Nucl. Instrum. Methods Phys. Res. A 600 (2009) 1–4, https://doi.org/10.1016/j.nima.2008.11.019.

[4] S. Nagamiya, Prog. Theor. Exp. Phys. 2012 (2012), https://doi.org/10.1093/ptep/pts025, 02B001.

[5] S. Wang, et al., Sci. China Phys. Mech. Astron. 54 (2011) 239–244, https://doi.org/10.1007/s11433-011-4564-x.

[6] J. Wei, et al., Chin. Phys. C 33 (2009) 1033–1042, https://doi.org/10.1088/1674-1137/33/11/021.

[7] V. Santoro, et al., J. Neutron Res. 22 (2020) 209–219, https://doi.org/10.3233/JNR-200159.

[8] J.W.G. Thomason, Nucl. Instrum. Methods Phys. Res. A 917 (2019) 61–73, https://doi.org/10.1016/j.nima.2018.11.129.

[9] G. Škoro, et al., Physica B 551 (2018) 381–385, https://doi.org/10.1016/j.physb.2017.12.060.

[10] M. Lindroos, et al., Nucl. Instrum. Methods Phys. Res. B 269 (2011) 3258–3260, https://doi.org/10.1016/j.nimb.2011.04.012.

[11] D. Filges, Handbook of Spallation Research: Theory, Experiments and Applications, Wiley-VCH, 2009, pp. 17–20.

[12] S. Sakamoto, Technical Design Report of Spallation Neutron Source Facility, J-PARC, JAEA-Technology-2011-035, 2012, pp. 465–467.

[13] S. Bauer, et al., in: Nuclear Non-proliferation in International Law: Volume II — Verification and Compliance, T.M.C. Asser Press, 2015, pp. 131–150.

[14] C. Doll, et al., J. Environ. Radioact. 255 (2022) 107036, https://doi.org/10.1016/j.jenvrad.2022.107036.

[15] P.W. Eslinger, et al., J. Environ. Radioact. 251 (2022) 106963, https://doi.org/10.1016/j.jenvrad.2022.106963.

[16] T. Mora, et al., J. Nucl. Sci. Technol. 55 (2018) 548–558, https://doi.org/10.1080/00223131.2017.1417173.

[17] V. Barkauskas, et al., Nucl. Instrum. Methods Phys. Res. B 471 (2020) 24–32, https://doi.org/10.1016/j.nimb.2020.03.013.

[18] Swedish Radiation Safety Authority, ESS research facility, Basis for Emergency Preparedness and Response Planning, 2018. Report No. 2018:22e.

[19] H. Liu, et al., Radiat. Detect. Technol. Meth. 6 (2022) 339–348, https://doi.org/10.1007/s41605-022-00325-5.

[20] S. Le Caër, Water 3 (2011) 235–253, https://doi.org/10.3390/w3010235.

[21] D.R. Walz, E.J. Seppi, Radiolysis and Hydrogen Evolution in the A-Beam Dump Radioactive Water System, SLAC-TN-67-29, SLAC, 1967.

[22] G. Battistoni, et al., AIP Conf. Proc. 896 (2007) 31–49.

[23] A. Fassò, et al., arXiv:hep-ph/0306267, 2003.

[24] U.S. Environmental Protection Agency, High Resolution Gamma-Ray Spectrometry Analyses for Normal Operations and Radiological Incident Response, 2019. EPA 402-B-17-001.

[25] L.A. Currie, Anal. Chem. 40 (1968) 586–593, https://doi.org/10.1021/ac60259a007.

[26] S. Wei, et al., Nucl. Eng. Technol. 54 (5) (2022) 1535–1540, https://doi.org/10.1016/j.net.2021.10.032.

[27] S.G. Lias, et al., NIST Chemistry Webbook, 69, NIST Standard Reference Database, 2005.

[28] G. Kastl, Modification of Water Treatment Processes for Chlorine Stability and Disinfection By-products Control, Ph.D. Thesis, Western Sydney University, 2019.

[29] R.C. Ropp, Encyclopedia of the Alkaline Earth Compounds, Elsevier, 2013, https://doi.org/10.1016/C2012-0-00777-6.

[30] R. Sander, Atmos. Chem. Phys. 15 (2015) 4399–4981, https://doi.org/10.5194/acp-15-4399-2015.

[31] J. Rest, et al., J. Nucl. Mater. 513 (2019) 310–345, https://doi.org/10.1016/j.jnucmat.2018.08.019.